Journal of Infrared, Millimeter, and Terahertz Waves (2023) 44:673–692
https://doi.org/10.1007/s10762-023-00938-x

Single-Mode Hollow-Core Anti-Resonant Waveguides for Low-Loss THz Wave Propagation

Lu Xue[1] · Xinzhi Sheng[1] · Qiyuan Mu[2] · Depeng Kong[2] · Zhaojin Wang[3] · Paul K. Chu[4] · Shuqin Lou[5]

Received: 27 May 2023 / Accepted: 14 August 2023 / Published online: 19 August 2023

Abstract

A single-mode hollow-core anti-resonant (HC-AR) waveguide designed for low-loss terahertz (THz) wave propagation is fabricated by three-dimensional (3D) printing. Compared to similar structures reported recently, the rotating-nested semi-elliptical tubes (SETs) in the HC-AR THz waveguide cladding suppress multiple high-order modes (LP_{11}, LP_{21}, and LP_{02} modes) at the same time giving rise to enhanced single-mode transmission and low losses. Three HC-AR THz waveguides with different wall thicknesses are produced using two photosensitive resins and analyzed by THz time-domain spectroscopy (THz-TDS). The experimental results show that the electric field distributions at the output end of these waveguides have a Gaussian-like distribution reflecting that of the single mode. The smallest transmission losses determined by the 'cut-back' method are 0.03 cm^{-1} at 0.31 THz for sample A, 0.02 cm^{-1} at 0.4 THz for sample B, and 0.01 cm^{-1} at 0.23 THz for sample C. The consistent experimental and simulated results reveal that the HC-AR THz waveguide has many advantages over current ones by achieving low losses and single-mode operation simultaneously.

Keywords Single mode · Hollow-core anti-resonant THz waveguide · THz time-domain spectroscopy

1 Introduction

The rapid development of terahertz (THz) technology is spurring the use of THz wave in the information transmission, imaging, sensing, security, and detection fields [1, 2]. As an important transmission medium of THz waves, THz waveguides have the advantages of low loss, wide bandwidth, and strong resistance to external interference. Various forms of THz waveguides have been reported and they can be generally divided into two categories, metallic waveguides and dielectric waveguides [3]. Metallic waveguides tend to have high intrinsic Ohmic losses and it is

Extended author information available on the last page of the article

difficult to couple THz waves into the waveguide, resulting in unavoidable dissipated heat and increased transmission losses [4–6]. With regard to dielectric waveguides, solid-core waveguides suffer from high absorption losses because of the large confinement of the modal power of the dielectrics [7–11]. Porous-core waveguides show reduced losses, but their complex structures render commercial manufacturing difficult [12–14]. Hollow-core waveguides offer an effective approach to realize low losses by confining most of the power in the air core to reduce the material loss [15–17]. Hence, hollow-core waveguides have received increasing attention in recent years due to the smaller transmission losses.

According to the guidance mechanism, there are two types of THz hollow-core waveguides. The first type is the hollow-core photonic bandgap (HC-PBG) THz waveguide, in which the light is guided inside the hollow core by the photonic bandgap effect [18]. In 2008, the first HC-PBG THz waveguide was composed of a set of concentric layers suspended in air by a network of circular bridges [19], and the total loss is less than 0.012 cm^{-1} (5 dB/m) at 0.8 THz. Xiao et al. have reported a quasi-elliptical-core HC-PBG THz waveguide with a confinement loss of 3×10^{-3} cm^{-1} at 0.9 THz [18]. However, the development of HC-PBG THz waveguides has been restricted by their narrow bandwidth, complex structure, low design flexibility, and manufacturing difficulty. Fortunately, these drawbacks plaguing HC-PBG THz waveguides can be overcome by another type of hollow-core THz waveguides, i.e., the hollow-core anti-resonant (HC-AR) THz waveguides, also known as inhibited-coupling hollow-core THz waveguides [20, 21]. The HC-AR THz waveguides have several distinct advantages such as a wider transmission window, lower loss, and manufacturing simplicity. In 2008, Lu et al. proposed the first Kagome HC-AR THz waveguide with a loss of less than 0.002 cm^{-1} at 0. 77 THz [22]. Recently, Talataisong et al. have fabricated an HC-AR THz waveguide with the Topas polymer by 3D printing showing a loss of 0.12 dB/cm (0.028 cm^{-1}) at 0.7 THz [20].

Besides low losses, the single-mode characteristics are important to THz waveguides for the transmission of THz waves. The losses can be further mitigated by increasing the core size. However, this optimization strategy introduces drawbacks such as the large total size, lower flexibility, and multimode regimes of operation. Therefore, when designing the geometry and dimensions of HC-AR THz waveguides, care must be taken to suppress the multiple high-order modes (HOMs) and improve the single-mode properties. For example, HC-AR THz waveguides can suppress the LP_{02} mode (HE_{12} mode) when eight polypropylene capillaries are introduced to the cladding [23] and the corresponding loss of the fundamental mode (FM) is 3.8 dB/m (8.7×10^{-3} cm^{-1}) at 2.15 THz. Sultana et al. have demonstrated a low-loss single-mode HC-AR THz waveguide with a nested cladding tube structure [24]. The loss of the FM is as low as 0.05 dB/m (1.2×10^{-4} cm^{-1}) at 1 THz, and multiple HOMs are suppressed. However, small fluctuations in the cladding tube size have a significant impact on the single-mode characteristics and increase the manufacturing difficulty. A Zeonex-based single-mode 7-tube HC-AR THz waveguide with an FM loss of 1.86×10^{-4} cm^{-1} at 1 THz has been proposed [25]. However, it is still in the research stage and has not been fabricated. Recently, our group designed a single-mode low-loss HC-AR THz waveguide with 6-semi-elliptical tubes to only suppress the LP_{11} mode [26].

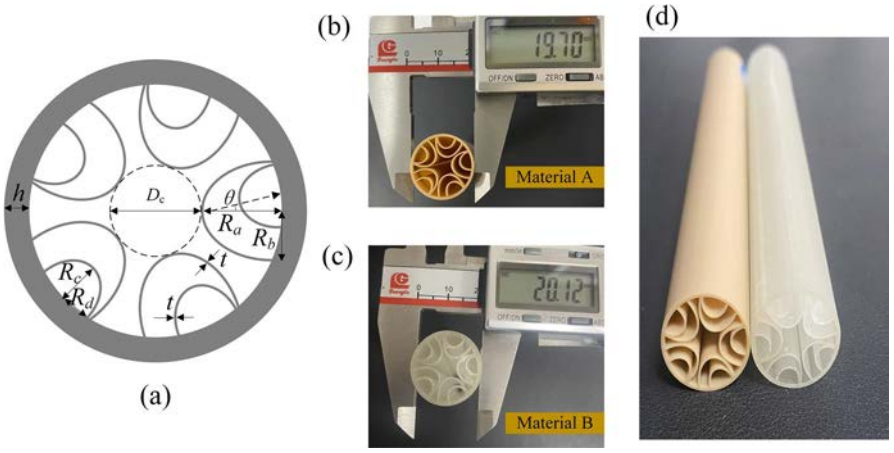

Fig. 1 **a** Cross-section of the HC- AR THz waveguide used in the simulation, **b**, **c** Cross-sections of the fabricated waveguides, and **d** Picture of the 3D-printed samples

The experimental results showed that the average loss was 0.048 cm^{-1} in the frequency range between 0.2 and 1 THz. Nonetheless, it is still important to improve the single-mode and low-loss transmission characteristics of HC-AR THz waveguides by optimizing the internal structure while also considering the manufacturing flexibility and reliability.

Herein, we design and demonstrate a low-loss single-mode transmission HC-AR THz waveguide comprising the rotating nested semi-elliptical tubes (SETs) as the cladding for simultaneous suppression of multiple HOMs (LP_{11}, LP_{21}, and LP_{02} modes). During three-dimensional (3D) printing, two photosensitive resins are adopted to fabricate three HC-AR THz waveguides with different wall thicknesses of SETs. The samples are characterized by THz time-domain spectroscopy (THz-TDS). The electric field measured at the output end of these waveguides exhibits a Gaussian-like distribution confirming single-mode propagation. And the low transmission losses can be obtained for these samples. The experimental and theoretical results are in good agreement.

2 Waveguide Structure and Parameters

Figure 1a depicts the cross-section of the HC-AR THz waveguide with the ideal 5-tube nested semi-elliptical tubes (SETs), in which the grey regions represent the dielectric materials and the white regions denote air. The nested SETs rotate at an angle θ relative to the outer SETs. The core diameter of the waveguide is D_c and the major and minor axes of the SETs and nested SETs are R_a, R_b, R_c, and R_d, respectively. The thickness of SETs is t, and the wall thickness of the outer circular tube as a mechanical protective layer is h.

Table 1 Dimensions of the fabricated HC-AR THz waveguides

Samples	A	B	C
Materials	Material A		Material B
D_c (mm)	5.62	5.62	5.62
t (mm)	0.3	0.39	0.3
R_a (mm)	6	6	6
R_b (mm)	4	4	4
R_c (mm)	3.4	3.4	3.4
R_d (mm)	2.6	2.6	2.6
θ	9°	7°	9°
h (mm)	0.89	0.8	0.89
Outside diameter (mm)	20	20	20
Length (mm)	50, 100	150, 190	100, 150

The HC-AR THz waveguides are fabricated with two photosensitive resins by 3D printing and the corresponding cross-sections are displayed in Fig. 1b and c. The yellow photosensitive resin is material A. The other is a transparent photosensitive resin designated as material B. The three HC-AR THz waveguides are prepared with material A with wall thicknesses t of 0.3 and 0.39 mm and material B with a wall thickness $t = 0.3$ mm. For simplicity, the HC-AR THz waveguides made of material A are labeled sample A ($t = 0.3$ mm) and sample B ($t = 0.39$ mm), while the ones fabricated with material B are designated sample C ($t = 0.3$ mm). The dimensions of the three waveguides are summarized in Table 1. Each sample has two different lengths in order to form longer waveguides, which will be discussed later. Furthermore, we analyze the selection of the two key parameters in Table 1, namely the wall thickness t and angle θ, which are introduced in Section 3.

3 Simulation

The finite element method (FEM) incorporating the perfect match layer (PML) is implemented to analyze the losses and single-mode characteristics of the waveguides. To guarantee convergence of the simulated results, both the mesh sizes and PML parameters are optimized. The mesh element size is not greater than 0.05 mm in the region of the photosensitive resin and air core, and less than 0.08 mm in the hollow regions of the cladding. The thickness of PML is 2.0 mm with a maximum mesh size of less than 0.2 mm.

The resonant frequencies of an anti-resonant waveguide are determined as follows [16]:

$$f_m = \frac{mc}{2t\sqrt{n^2 - 1}}, \tag{1}$$

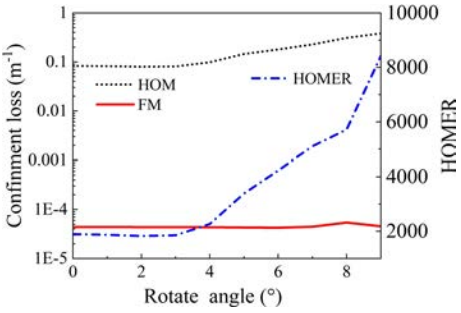

Fig. 2 Lowest confinement loss of the HOMs, confinement loss of FM, and HOMER as a function of the rotation angle θ

where c is the speed of light in vacuum, t is the wall thickness of the anti-resonant waveguide, n is the real part of the refractive index of the photosensitive resin, and m is an integer. The transmission loss includes the effective material loss (α_{eff}) and confinement loss (α_{c}) and α_{eff} can be estimated as follows [3]:

$$\alpha_{\text{eff}} = \frac{(\varepsilon_0/\mu_0)^{1/2}\int_{A_{\text{mat}}} n\alpha_{\text{mat}}|E|^2 dA}{2\int_{\text{All}} S_Z dA}, \tag{2}$$

where ε_0 and μ_0 are the permittivity and permeability in vacuum, respectively, α_{mat} is the bulk absorption loss of the photosensitive resin, and n is the real part of the refractive index of the photosensitive resin. The properties of the photosensitive resin will be discussed in Section 4.1. Here, S_z is defined as the Poynting vector in the propagation direction z and equal to 1/2×Re(E×H^*) z, in which E is the electric field component and H is the magnetic field component. Integration of the numerator in Eq. (2) is performed over the region of the photosensitive resin and integration of the denominator is done for all the waveguide regions. α_{c} can be calculated by the following expression [3],

$$\alpha_c = (\frac{4\pi f}{c})\text{Im}(n_{\text{eff}}), \tag{3}$$

where f is the operating frequency and Im(n_{eff}) is the imaginary part of the effective index n_{eff} of the guided mode. In theory, the wall thickness t should be as small as possible to achieve a broad transmission band.

In our case, the wall thickness is limited to 0.3 mm by our 3D printer. Therefore, we chose the wall thickness t of 0.3 mm for the low loss and relatively wide transmission band. In addition, in order to compare the transmission characteristics of waveguides with different wall thicknesses, another waveguide with a wall thickness of 0.39 mm is printed and analyzed.

To keep the nested SETs inside the cladding tubes, θ is changed from 0° to 9°. The lowest confinement loss of the HOMs, confinement loss of FM, and HOMER as a function of the rotation angle θ are shown in Fig. 2. The high-order mode extinction ratio (HOMER), which is defined as the ratio of the lowest confinement loss of HOMs to the confinement loss of FM, is employed to evaluate the single-mode transmission performance of the waveguides. A higher HOMER indicates better

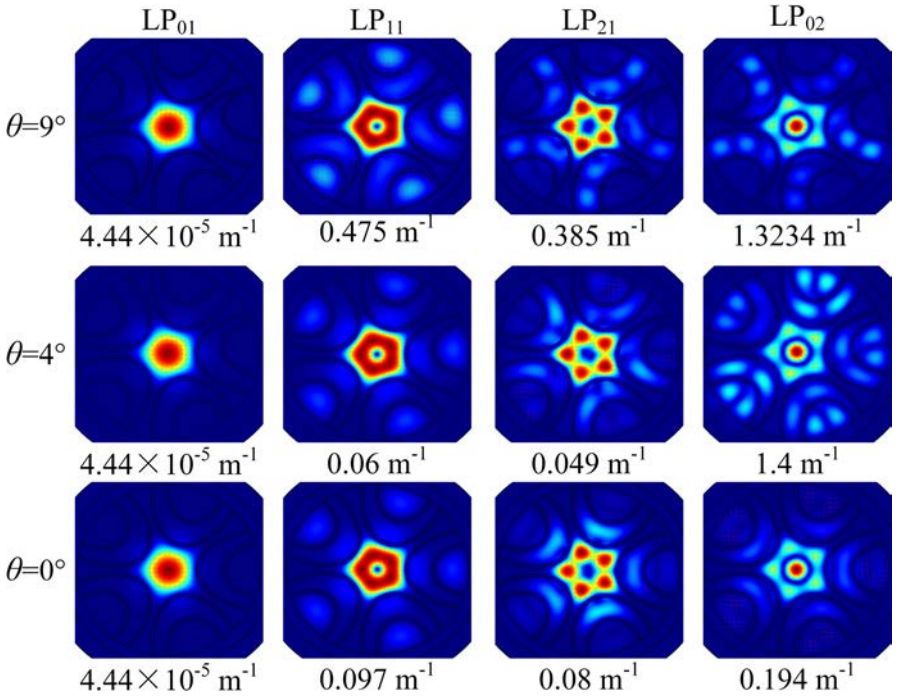

Fig. 3 Mode field distributions and confinement losses of the LP_{01}, LP_{11}, $LP_{21,}$ and LP_{02} modes at the rotation angles θ of 0°, 4°, and 9° at 0.6 THz, respectively

single-mode characteristics. It can be seen that the confinement loss of FM is nearly constant for θ between 0° and 9°. The lowest confinement loss of HOMs is 3 orders of magnitude higher than that of FM and therefore, a high HOMER is ensured. The HOMER increases rapidly from 1894 at $\theta=0°$ to 8413 at $\theta=9°$, as shown in Fig. 2. The mode field distributions and confinement losses of FM (LP_{01} mode) and HOMs (LP_{11}, $LP_{21,}$ and LP_{02} modes) are shown in Fig. 3 for $\theta=0°$, 4° and 9° at 0.6 THz, respectively. It is remarkable that the energy of FM is confined in the hollow core very well, while the energy of HOMs partly expands into the cladding tubes. There represents a distinctive enhancement in the intensity profile of the cladding tubes for HOMs at $\theta=9°$ due to strong coupling between the HOMs and cladding modes (CMs). Therefore, we choose $\theta=9°$ for the single-mode low-loss guidance.

The structures shown in Table 1 are used to simulate the transmission characteristics of the waveguides. The refractive index n_B of material B is measured by the THz-TDS system and will be discussed in Section 4.1. Figure 4 shows the simulated effective refractive index (n_{eff}) and loss of FM of sample C when f is scanned from 0.15 to 1.0 THz. As expected, there are two loss peaks at 0.39 THz and 0.75 THz in the frequency range between 0.15 and 1.0 THz, which are consistent with the theoretical resonant frequencies for $m=1$ and $m=2$ in the grey region from Eq. (1) when $t=0.3$ mm and $n_B = 1.6778$. The corresponding changes around the resonant frequencies can also be observed from the effective refractive index curve in Fig. 4b. Similar

Table 2 Structures of the four THz waveguides

Waveguide	D_c (mm)	D	d (mm)	t (mm)	R_a (mm)	R_b (mm)	R_c (mm)	R_d (mm)	Refs.
I	5.6	-	-	0.3	6	4	3.4	2.9	-
II	5.6	0.68* D_c	-	0.3	-	-	-	-	[28]
III	5.6	-	-	0.3	3.75	2.21	-	-	[26]
IV	5.6	1.09* D_c	4.17	0.3	-	-	-	-	[24]

transmission characteristics are observed from samples A and B. At the same time, the FM is confined in the hollow core of the three samples, as shown in Fig. 5.

The bending characteristics of waveguides are important in practical applications. Bending produces anisotropy in the waveguides and so the characteristics of waveguides can be affected. In the simulation, a bent waveguide is typically equivalent to a straight waveguide with an equivalent refractive index distribution expressed as follows [24]:

$$n(x, y) = n_0(x, y)(1 + v/R_{bend}), \tag{4}$$

where (x, y) are the coordinates with the origin at the center of the waveguide, n (x, y) is the equivalent refractive index distribution of the bent waveguide, n_0 (x, y) is the original refractive index distribution of the straight waveguide, and R_{bend} is the bending radius toward the v-direction, and v stands for the x and y bending directions shown in Fig. 6a.

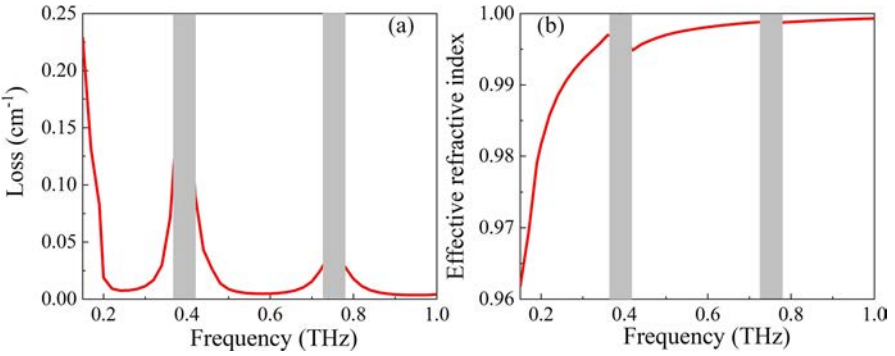

Fig. 4 **a** Loss and **b** Effective refractive index as a function of frequencies of sample C

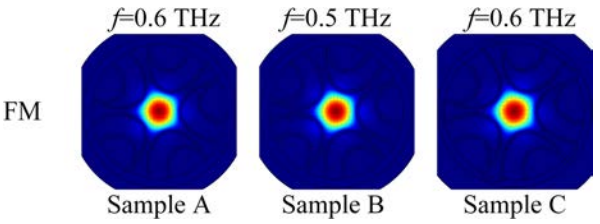

Fig. 5 Electric filed distributions of the FM of samples A, B, and C

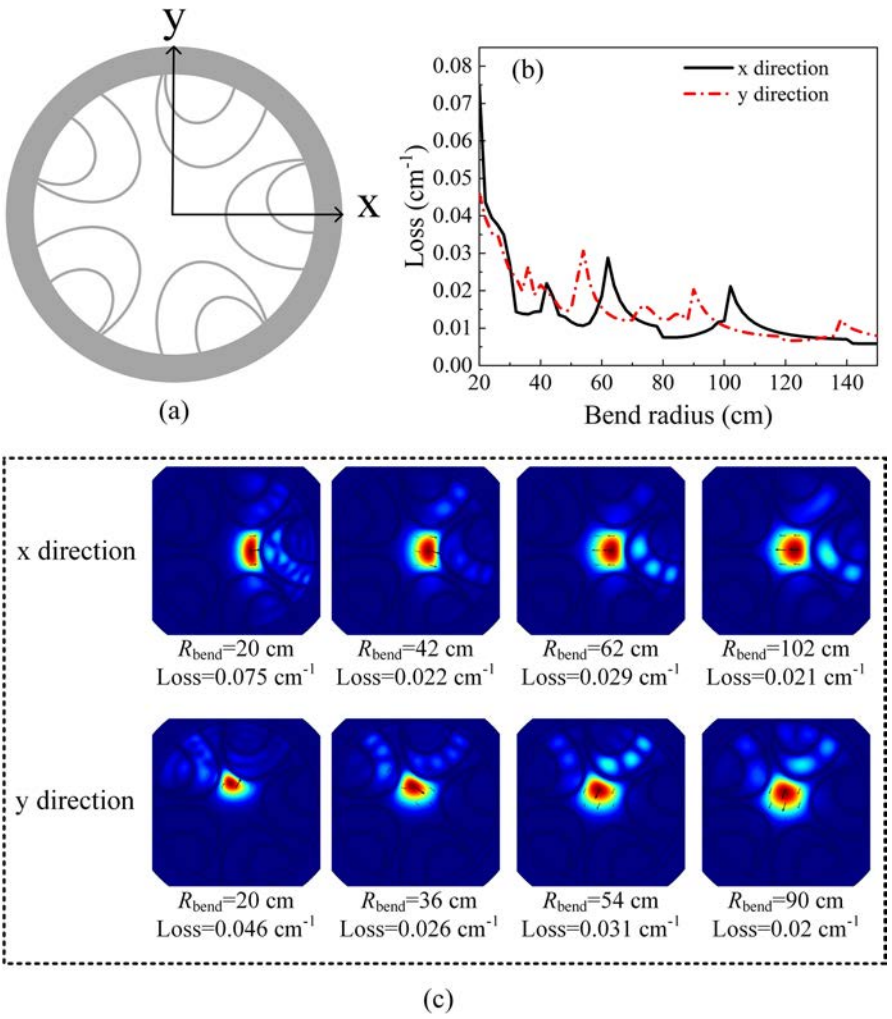

Fig. 6 **a** Bending direction, **b** Loss as a function of the bending radius of sample C in the *x* and *y* bending directions at 0.6 THz, and **c** Electric filed distributions and loss of the FM at 0.6 THz for different bending radii in the *x* and *y* bending directions

Figure 6b displays the transmission loss of sample C as a function of the bending radius at a frequency of 0.6 THz. According to numerical simulation, for $R_{bend} <$ 30 cm, the waveguide exhibits high bending losses in different bending directions. For ease of visualization, Fig. 6c includes the mode field distributions of the FM at $R_{bend} = 20$ cm for the *x* and *y* bending directions at 0.6 THz. For 30 cm $< R_{bend} <$ 150 cm, the FM loss decreases with bending radius. However, the bending loss spectra of the FM show undesired high loss peaks when 30 cm $< R_{bend} <$ 150 cm. For example, the high loss peaks of 0.022 cm^{-1}, 0.029 cm^{-1}, and 0.021 cm^{-1} appear at about $R_{bend} = 42$ cm, 62 cm, and 102 cm for the *x* bending direction at 0.6 THz,

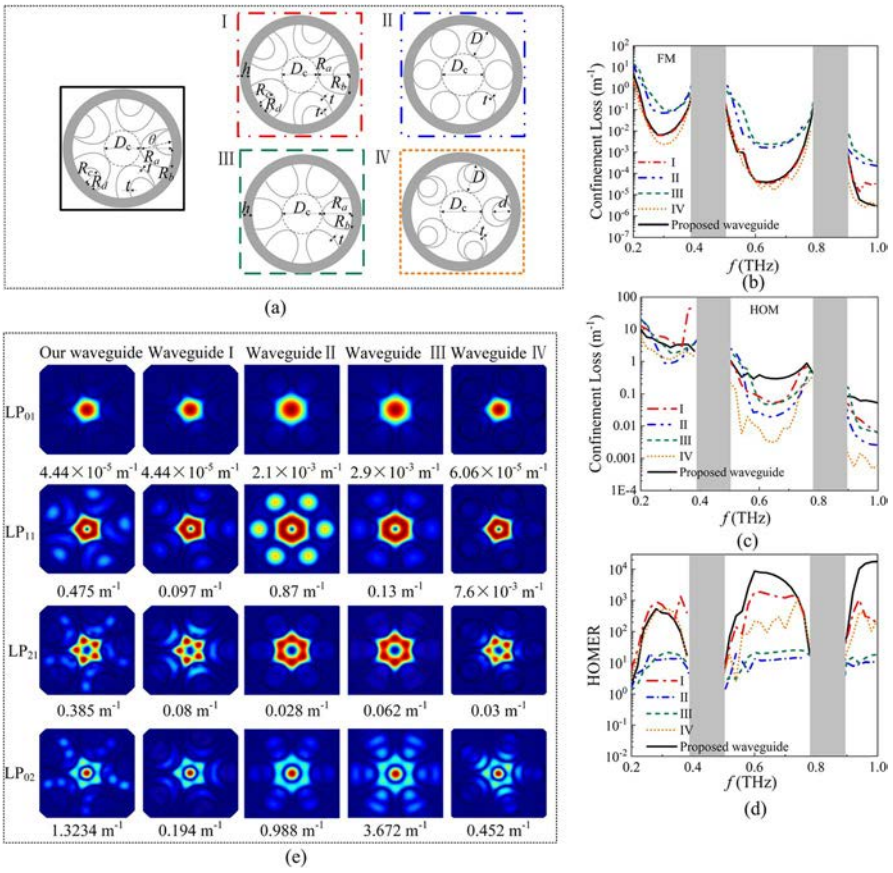

Fig. 7 **a** Cross-sections, **b** Confinement losses of FM, **c** Lowest confinement losses of HOMs, **d** HOMER, and **e** Mode field distributions and confinement losses of the LP_{01}, LP_{11}, $LP_{21,}$ and LP_{02} modes at 0.6 THz of the five SM HC-AR THz waveguides

respectively. The high-loss peaks of 0.026 cm^{-1}, 0.031 cm^{-1}, and 0.02 cm^{-1} appear at around $R_{\text{bend}} = 36$ cm, 54 cm, and 90 cm for the y bending directions at 0.6 THz, respectively. The mode field distributions corresponding to these high-loss peaks are shown in Fig. 6c, and it can be clearly seen that the core mode leaks into the semielliptical cladding tube gap.

Several types of single-mode HC-AR THz waveguides have been reported [23–27]. In order to evaluate the performance of our structure, we compare four single-mode HC-AR THz waveguides as shown in Fig. 7a, namely, the 5-tube nested SETs HC-AR THz waveguide with $\theta = 0°$, 6-tube HC-AR THz waveguide [28], 6-tube SETs HC-AR THz waveguide [26, 27], and 5-tube nested HC-AR THz waveguide [24]. The geometries of four single-mode HC-AR THz waveguides are shown in Fig. 7a and referred to as waveguide I, waveguide II, waveguide III, and waveguide IV. The diameter of the core is D_c and the outer cladding tube diameter and

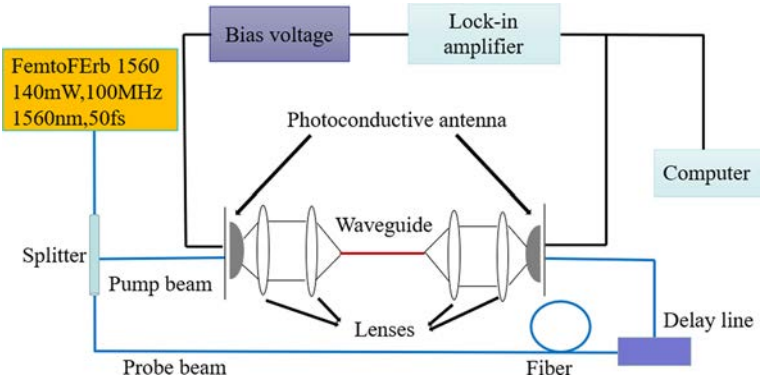

Fig. 8 Schematic of the THz-TDS setup

nested cladding tube diameter are D and d, respectively. The wall thickness of the cladding tube is t. The refractive index n_A of material A is 1.6265 (to be discussed in Section 4.1) and the structural parameters are listed in Table 2.

The transmission properties of our 5-nested SETs HC-AR THz waveguide and four other structures are shown in Fig. 7. Figure 7b presents the confinement loss spectra of FM for the different structures as a function of frequencies. Our HC-AR THz waveguide has a similar low confinement loss of FM as waveguides I and IV within the transmission bandwidth due to the inner nested tube elements. On the other hand, waveguides II and III have higher confinement losses of FM than our waveguide because there are no inner nested tube elements. As shown in Fig. 7c, within the transmission bandwidth, the lowest confinement loss of HOMs (LP_{11}, LP_{21}, and LP_{02} modes) of our waveguide is the highest. Therefore, the 5-nested SETs HC-AR THz waveguide has the biggest HOMER as shown in Fig. 7d. A higher HOMER indicates better single-mode characteristics and thence, our HC-AR THz waveguide delivers excellent single-mode performance in the transmission bandwidth. Figure 7e displays the mode field distributions and confinement losses of the LP_{01}, LP_{11}, LP_{21}, and LP_{02} modes for the different single-mode HC-AR THz waveguides at 0.6 THz. Figure 7e shows that the LP_{01} mode can be confined in the hollow core giving rise to low confinement loss of the LP_{01} mode for all the HC-AR THz waveguides. However, the LP_{11}, LP_{21}, and LP_{02} modes show high confinement losses at the same time for our THz waveguide due to the strong coupling with the corresponding cladding modes.

4 Experimental Results

4.1 Properties of the Waveguide Material

In order to make a precise and quantitative comparison between the experimental and simulation results, the bulk dielectric properties (attenuation coefficient and refractive index) of material A and material B are determined by THz

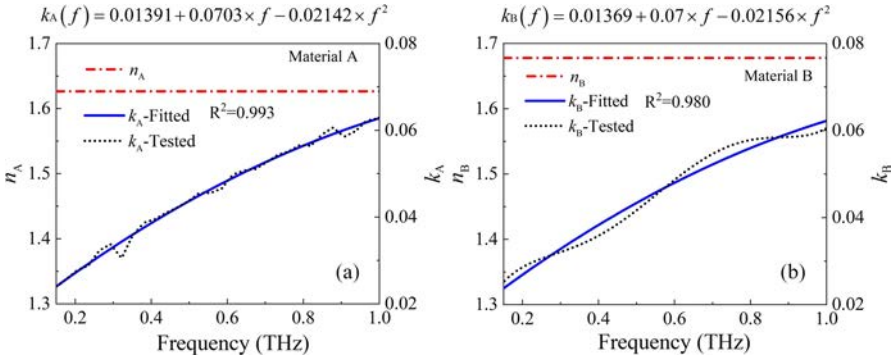

Fig. 9 Dielectric properties of **a** Material A and **b** Material B as a function of frequencies

time-domain spectroscopy (THz-TDS). The standard free-space THz-TDS setup depicted in Fig. 8 is used to measure the properties of the photosensitive resin materials and waveguides. To ensure that a constant amount of light is coupled to the sample, the THz beam is collimated and focused with polymer symmetric-pass (s-p) lenses. The sample is mounted on a customized holder which includes two apertures and clamps to fix the sample at the focal point of the s-p lenses.

The samples with a thickness of 1.08 mm and a diameter of 13 mm are prepared by a 3D printer. A reference comparison method is used to obtain the dielectric properties ($\widetilde{n} = n + ik$) of the materials, where n is the real part corresponding to the refractive index and k is the imaginary part related to the attenuation coefficient α_{mat} of the materials. In the THz-TDS system, the time-domain pulse signals with and without the sample are measured first, and then the frequency-domain signals are deduced by performing fast Fourier transform (FFT) to the time-domain signals. Therefore, both the signal phase φ and the electric field component E as a function of the frequencies are resolved. By comparing the signal phase delay $\Delta\varphi$ and intensity change with the reference signal, the real part n and the attenuation coefficient α_{mat} of the materials can be determined as below [15]:

$$n = \frac{\Delta\varphi c}{2\pi f L} + 1 \tag{5}$$

$$\alpha_{mat} = \frac{2\ln(E_{\text{sam}}/E_{\text{ref}})}{L}, \tag{6}$$

where $\Delta\varphi = \varphi_{\text{sam}} - \varphi_{\text{ref}}$ indicates the phase difference between the sample and reference signal, L is the thickness of the sample, c is the speed of light in vacuum, f is the frequency of the THz signal, E_{sam} and E_{ref} are the electric field component of the sample and reference signal, respectively. The imaginary part k refers to the extinction coefficient calculated in terms of the attenuation coefficient α_{mat} as follows [15]:

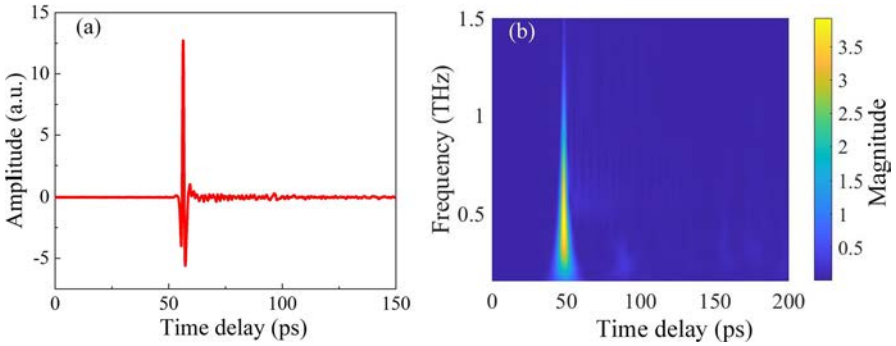

Fig. 10 **a** Time-domain reference signal and **b** Corresponding spectrogram of the THz emitter

Fig. 11 Photographs of the connected waveguides

$$k = \frac{\alpha_{mat} c}{4\pi f} \tag{7}$$

Figure 9 shows the dielectric properties of materials A and B. The refractive indexes n of both materials are nearly constant, and the extinction coefficients k increase monotonically with frequencies. The refractive indexes n measured from the materials n_A and n_B are 1.6265 and 1.6778, respectively. The extinction coefficients k are smoothed by fitting the experimental data with a simple polynomial represented by the blue solid curves in Fig. 9. The fitted expressions and parameters shown in the corresponding figures are used in the simulation, and R^2 of k_A and k_B are 0.993 and 0.980, respectively.

4.2 Temporal Evolution

To confirm the THz guidance in the HC-AR THz waveguides, they are characterized by THz-TDS. While keeping a constant distance between the detector and transmitter, the reference signal is scanned without the optical waveguide. The time domain reference signals are shown in Fig. 10a and the spectrograms in Fig. 10b are derived from the measured time traces of the electric field of the THz output pulses using the continuous wavelet transform. The spectrogram of the THz emitter indicates that the THz pulse aggregates at about the arrival time of 50 ps. The strongest intensity appears at f~0.4 THz and the effective bandwidth of the THz emitter covers the frequency range between 0.1 THz and 1.3 THz.

Since the maximum length of the waveguide is restricted by the working distance of the 3D printer, it is difficult to make long waveguides. However, long waveguides can be made by connecting two of them in series as shown in Fig. 11. Figure 12 presents the temporal THz waveforms of sample B for $t=0.39$ mm and three different lengths of 150 mm, 190 mm, and 340 mm. The THz pulse passes through the longer waveguide (340 mm long), arrives at the detector at 1,189 ps, and propagates along the shorter

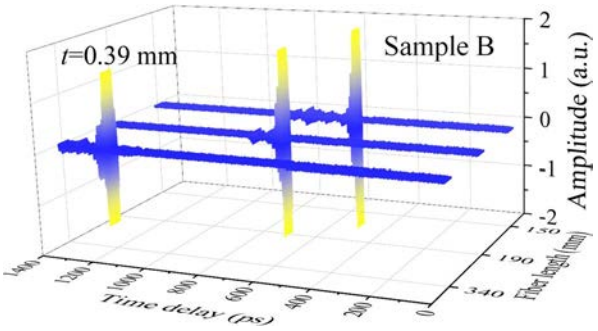

Fig. 12 Temporal profiles of THz waves after propagation through different lengths in sample B

Table 3 Comparison of different THz waveguides reported recently

Waveguide Model	Mode Purity	Materials	Core Diameter (mm)	Simulated Loss (cm^{-1})	Experimental Loss (cm^{-1})	Operating Frequencies (THz)	Refs.
	Single-mode	COC	3.10	0.012 (5 dB/m)	0.007 (3 dB/m)	0.9	[16]
	-	COC	2.2	-	0.028 (0.12 dB/cm)	0.7	[20]
	Single-mode	PP	2.86	-	0.017 (7.4 dB/m)	2.15	[23]
	-	Polylactic acid	30	0.009	0.015	0.1	[30]
	Single-mode	UV-curable polymer and copper wires	3	0.2	0.2	1.0	[5]
	Single-mode	ABS plastic and copper coatings	5	-	0.002 (0.85 dB/m)	0.98	[31]
	Single-mode	Polycarbonate	10	0.008 (0.033 dB/cm)	0.018 (0.08 dB/cm)	0.3	[27]
	Single-mode	Photosensitive resin	7	2.9×10^{-3}	9×10^{-3}	0.6	[26]
	Single-mode	Photosensitive resin	5.62	0.008	0.01	0.23	This study

waveguide (150 mm long) at about 563 ps. When the waveguide is longer, the signal amplitude drops, and no additional pulses appear behind the main one, indicating the absence of HOMs in our waveguide. The temporal waveforms of the other show similar features as sample B. The quantitative discussion of the HOMs of the waveguide will be discussed later in the following sections.

4.3 Single-Mode Characteristics

The electric field distribution, which is an important basis to verify the single-mode operation of waveguides, is determined by the 'knife-edge' method [26]. The metal plate fixed on the displacement platform is placed at the waveguide output end and moved by 0.25 mm per step. The electric field amplitude in each step can be obtained by the difference of the THz amplitudes after and before each step. By this method, the normalized electric field distributions at the output end of the long samples A, B, and C are measured and displayed in Fig. 13. The label X on the coordinate axis is the displacement distance of the metal plate. The square dots are the experimental data acquired from samples A, B, and C. Nonlinear fitting is performed on the experimental data and shown by the red solid curves in Fig. 13, and the fitted expressions and parameters are shown in the corresponding figures. There are three non-linear regions with R^2 of 0.968, 0.927, and 0.963 respectively. The electric field profiles of the three samples are Gaussian-like. The normalized electric field distributions of samples A, B, and C obtained by simulation are shown by the blue dash curves in Fig. 13. The experimental data are in good agreement with the simulated results as both have the Gaussian shape, indicating that all the three waveguide samples have the effective single-mode operation.

4.4 Transmission Losses

The transmission losses of the three waveguides are assessed by the standard 'cut-back' method. The waveguides are lengthened by connecting two short ones in series as aforementioned. The lengths are 100 and 150 mm for sample A, 190 and 340 mm for sample B, and 150 and 250 mm for sample C. Three measurements

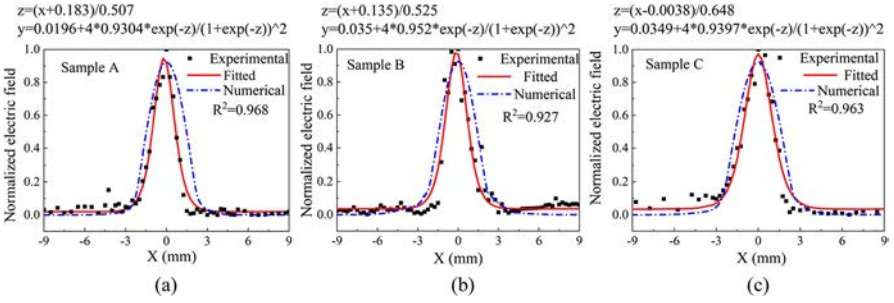

Fig. 13 Experimental and simulation results of the normalized electric field distributions at the output end of **a** Sample A, **b** Sample B, and **c** Sample C

are carried out and the average values are adopted to reduce the effect of the difference in coupling for each measurement. The comparison between the measured (red dotted line) and simulated (black soild line) losses of the three waveguides is exhibited in Fig. 14. Compared to the numerical results, the experimental loss peaks appear to red-shift because the wall thickness is slightly larger than the intentional value.

The effects of the wall thickness t of the waveguide made of material A on losses are investigated as shown in Fig. 14a and b. When t is increased from 0.3 to 0.39 mm, the loss peaks shift to lower frequencies, causing a shift in the transmission window. The resonant frequencies corresponding to the loss peaks are inversely proportional to the wall thickness t. Hence, to achieve low losses at specific frequencies, different wall thicknesses are evaluated. The measured transmission bandwidths with losses less than 0.1 cm^{-1} are 0.4 THz for sample A ($t=0.3$ mm) and 0.55 THz for sample B ($t=0.39$ mm). The smallest losses are 0.03 cm^{-1} at 0.31 THz for sample A ($t=0.3$ mm) and 0.02 cm^{-1} at 0.4 THz for sample B ($t=0.39$ mm), all of which are about three orders of magnitude less than that of the bulk materials (10 cm^{-1}). The simulated transmission bandwidths with losses less than 0.1 cm^{-1} are 0.75 THz for sample A ($t=0.3$ mm) and 0.76 THz for sample B ($t=0.39$ mm). The simulated smallest losses are 0.003 cm^{-1} and 0.06 cm^{-1} at 1 THz for $t=0.3$ and 0.39 mm, respectively.

We then investigate the effects of the materials on the losses. As shown in Fig. 14a (Material A) and Fig. 14c (Material B), as n increases from 1.6265 to 1.6778, the loss peaks shift slightly to lower frequencies thus altering the transmission window. The resonant frequencies corresponding to the loss peaks are also inversely proportional to n. Therefore, in order to accomplish low losses at different frequencies, besides changing the wall thickness t, different materials can be chosen. Similarly, the measured and simulated transmission bandwidths with losses less than 0.1 cm^{-1} are 0.45 THz and 0.73 THz for sample C (Material B), respectively. The measured and simulated lowest losses are 0.01 cm^{-1} at 0.23 THz and 0.004 cm^{-1} at 1 THz for sample C (Material B). The results are consistent with the observed losses found from sample A, because the k values of the two materials are basically consistent. The measured losses are less than the losses of the fabricated materials. The absorption range of the materials is from 1 cm^{-1} to 30 cm^{-1} between 0.15 THz and 1 THz. Therefore, by comparing the absorption losses of the materials, the losses of the

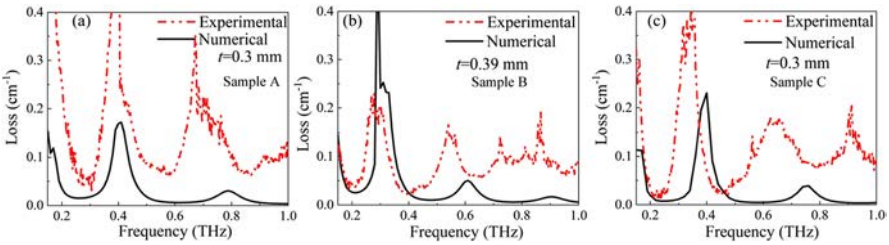

Fig. 14 Transmission losses of the experimental and simulation results for **a** Sample A, **b** Sample B, and **c** Sample C

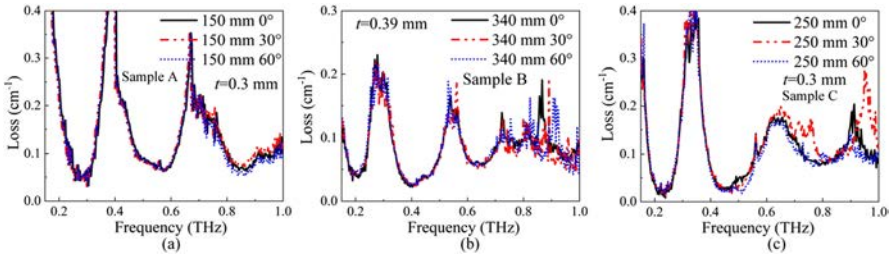

Fig. 15 Losses of **a** Sample A, **b** Sample B, and **c** Sample C using different cascade methods measured by THz-TDS experimentally

HC-AR THz waveguide can be reduced by at least an order of magnitude since the guided mode is confined in the air core region. In future research, it is advisable to choose materials with lower absorption losses to fabricate waveguides [29] in order to further reduce the transmission losses. There is some mismatch in some resonant frequencies between the simulated and experimental results attributable to the coupling loss in the experimental measurement and imperfect sample preparation.

Since the long sample is formed by connecting two short samples, the effects of misalignment on losses are evaluated. The two short samples are aligned but offset at angles of 0°, 30°, and 60°. The corresponding losses are shown in Fig. 15. In spite of the misalignment, samples A, B, and C only show small changes at frequencies less than 0.7 THz. This is because the waveguides with different structures and materials confine most of the THz waves in the hollow core, and there is almost no leakage to the cladding. Therefore, the dislocation of the cladding has little effect on the losses. Moreover, the deviation between the aligned angle (0°) and misaligned angles (30° and 60°) at high frequencies increases, perhaps because the signal drops to the noise level.

4.5 Dispersion

The effective refractive indexes and dispersion of the experimental and simulation results for sample A as a function of frequencies are shown in Fig. 16. As shown in

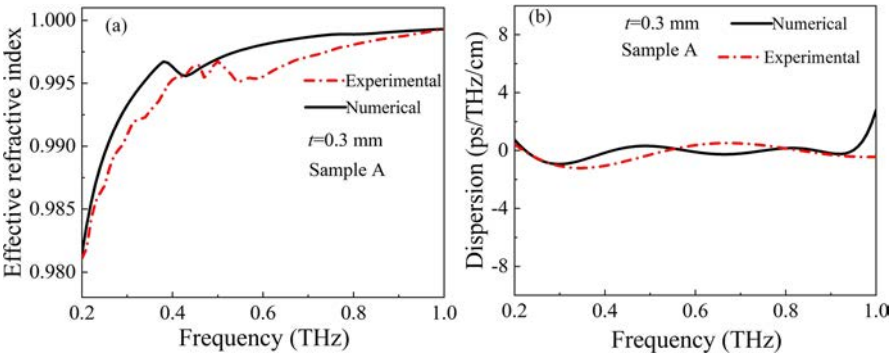

Fig. 16 **a** Effective refractive indexes and **b** Dispersion of the experimental and simulation results of Sample A

Fig. 16a, the effective refractive index increases smoothly as the frequency increases and approaches the air index except for a sudden change at the resonance frequencies due to energy leakage. The second derivative of the effective refractive index is related to the dispersion. We adopt the dispersion parameters commonly used in the optics regime to describe pulse broadening to reflect the significance of ultra-wideband propagation of THz waves. As shown in Fig. 16b, the experimental data show, on average, a dispersion magnitude on the order of ± 2 ps/THz/cm in the frequency range of 0.2 to 1.0 THz. The comparison between the experimental and simulated results is presented in Fig. 16 and the simulated results are in good agreement with the experimental results, validating the appropriateness of the tests and simulations. Furthermore, similar dispersion characteristics are observed from samples B and C. More importantly, the data strongly indicate comparable low dispersion propagation in our hollow core configurations.

4.6 Comparison

A comparison of recently reported THz waveguides that have been fabricated is shown in Table 3. Among the different THz waveguides, those described in Refs. [16, 20, 23, 30] have relatively low losses, but these waveguides either do not operate in the single mode or lack experimental confirmation of the single-mode characteristics. Although the THz waveguides in Refs. [5, 31] are operated in the single mode, the metals make manufacturing complicated. Although the 6 SETs THz waveguides described in Refs. [26, 27] exhibit lower losses and can enable single-mode propagation by efficient coupling, the structure offers limited flexibility to optimize the loss differentiation between the FM and HOMs, resulting in multimode interferences. Hence, only the LP_{11} and LP_{02} modes are suppressed, but not the LP_{21} mode. This is verified by our simulation shown in Fig. 7. In contrast, the geometry of the nested SETs HC-AR THz waveguide offers more leeway to manipulate mode transmission, thereby realizing low propagation losses of the FM and large loss discrimination between the FM and its HOMs simultaneously and resulting in strong mode selectivity. The experimental results demonstrate that our HC-AR THz waveguide indeed has many advantages pertaining to low-loss and single-mode operations.

5 Conclusion

A single-mode HC-AR THz waveguide is designed and fabricated by 3D printing using two types of photosensitive resins. Compared to similar structures reported recently, the rotating-nested SETs in the HC-AR THz waveguide cladding suppress multiple HOMs (LP_{11}, LP_{21}, and LP_{02} modes) at the same time to improve the single-mode transmission performance and lower the losses. To overcome the limitation of 3D printer, long samples are constructed by connecting two short ones in series. The electric field distributions at the output end of the waveguides exhibit the Gaussian-like distribution of the FM, thus verifying the single-mode characteristics.

The transmission losses determined by the standard 'cut-back' method between 0.15 and 1 THz indicate that the wall thickness and materials are the main factors affecting the anti-resonant frequencies and most of the THz power is confined in the core region. The transmission bandwidths with losses of less than 0.1 cm^{-1} of samples A, B, and C are 0.4 THz, 0.55 THz, and 0.45 THz, respectively. Furthermore, the lowest transmission losses are 0.03 cm^{-1} at 0.31 THz for sample A, 0.02 cm^{-1} at 0.4 THz for sample B, and 0.01 cm^{-1} at 0.23 THz for sample C. The measured transmission losses are in good agreement with simulated values across the entire bandwidth of our THz-TDS setup.

Author Contributions Lu Xue: Conceptualization, Simulation, Experimental test, Data processing, Writing original draft.Xinzhi Sheng: Conceptualization, Supervision. Qiyuan Mu and Depeng Kong: Waveguide fabrication.Zhaojin Wang: Resources providing.Paul Kim Ho Chu: Supervision, Writing – editing. Shuqin Lou: Supervision, Writing – review & editing.

Funding The work was supported by the National Natural Science Foundation of China (Grant No. 12174022), Beijing Municipal Natural Science Foundation (Grant No. 1232028), City University of Hong Kong Donation Research Grants (Nos. DON-RMG 9229021 and 9220061), as well as City University of Hong Kong Strategic Research Grant (SRG, No. 7005505).

Data Availability Data underlying the results presented in this paper are not publicly available at this time but may be obtained from the authors upon reasonable request.

Declarations

Ethical Approval Not applicable.

Competing Interests The authors declare no competing interests.

References

1. B. You and J.-Y. Lu, "Remote and in situ sensing products in chemical reaction using a flexible terahertz pipe waveguide," Opt. Exp., vol. 24, no. 16, pp. 18013–18023, 2016.
2. D. M. Mittleman, "Twenty years of terahertz imaging" Opt. Exp., vol. 26, no. 8, pp. 9417–9431, 2018.
3. J. Luo, S. Chen, H. Qu, Z. Su, L. Li, and F. Tian, "Highly birefringent single-mode suspended-core fiber in terahertz regime," J. Lightwave Technol., vol. 36, no. 16, pp. 3242–3248, 2018.
4. B. Bradley, H. James A., and M. Oleg, "Silver/polystyrene-coated hollow glass waveguides for the transmission of terahertz radiation," Opt. Lett., vol. 32, no. 20, pp. 2945–2947, 2007.
5. N. Yudasari, J. Anthony, and R. Leonhardt, "Terahertz pulse propagation in 3D-printed waveguide with metal wires component," Opt. Exp., vol. 22, no. 21, pp. 26042–54, 2014.
6. M. Navarro-Cia, M. S. Vitiello, C. M. Bledt, J. E. Melzer, J. A. Harrington, and O. Mitrofanov, "Terahertz wave transmission in flexible polystyrene-lined hollow metallic waveguides for the 2.5-5 THz band," Opt. Exp., vol. 21, no. 20, pp. 23748–23755, 2013.
7. W. Talataisong et al., "Novel method for manufacturing optical fiber: extrusion and drawing of microstructured polymer optical fibers from a 3D printer," Opt. Exp., vol. 26, no. 24, pp. 32007–32013, 2018.
8. M. Rozé, B. Ung, A. Mazhorova, M. Walther, and M. Skorobogatiy, "Suspended core subwavelength fibers: towards practical designs for low-loss terahertz guidance," Opt. Exp., vol. 19, no. 10, pp. 9127–9138, 2011.
9. G. Xu, K. Nallappan, Y. Cao, and M. Skorobogatiy, "Infinity additive manufacturing of continuous microstructured fiber links for THz communications," Sci. Rep., vol. 12, no. 1, pp. 1–13, 2022, Art. no. 4551.

10. M. Weidenbach et al., "3D printed dielectric rectangular waveguides, splitters and couplers for 120 GHz," Opt. Exp., vol. 24, no. 25, pp. 28968–28976, 2016.
11. M. Taherkhani, R. A. Sadeghzadeh, J. Taiber, J. Ornik, and M. Koch, "The Effect of Humidity and Temperature on Dielectric Fibre–Bound THz Transmission," J Infrared Millim. TE, vol. 40, no. 11–12, pp. 1092–1102, 2019.
12. Y. S. Lee et al., "Low-loss polytetrafluoroethylene hexagonal porous fiber for terahertz pulse transmission in the 6G mobile communication window," IEEE Trans. Microwave Theory Tech., vol. 69, no. 11, pp. 4623–4630, 2021.
13. S. Mei et al., "A porous core Zeonex THz fiber with low loss and small dispersion," *Opt. Fiber Technol*, vol. 69, Art. no. 102834, 2022.
14. K. Nielsen, H. K. Rasmussen, A. J. L. Adam, P. C. M. Planken, O. Bang, and P. U. Jepsen, "Bendable, low-loss Topas fibers for the terahertz frequency range," Opt. Exp. vol. 17, no. 10, pp. 8592–8601, 2009.
15. L. Xue et al., "High-birefringence low-loss hollow-core THz waveguide embedded parallel slab cladding," IEEE Trans. Terahertz Sci., vol. 12, no. 5, pp. 1–10, 2022.
16. N. Phanchat et al., "Extruded TOPAS hollow-core anti-resonant fiber optimized for THz guidance at 0.9THz," Opt. Exp., vol. 30, no. 8, pp. 13059–13069, 2022.
17. Y. Jing et al., "3D printed low-loss THz waveguide based on Kagome photonic crystal structure," Opt. Exp., vol. 24, no. 20, pp. 22454–22460, 2016.
18. H. Xiao, H. Li, B. Wu, and S. Jian, "Polarization-maintaining terahertz bandgap fiber with a quasi-elliptical hollow-core," Opt. Laser Technol., vol. 105, pp. 276–280, 2018.
19. A. Hassani, A. Dupuis, and M. Skorobogatiy, "Porous polymer fibers for low-loss Terahertz guiding," Opt. Exp., vol. 16, no. 9, pp. 6340–6351, 2008.
20. W. Talataisong et al., "Hollow-core antiresonant terahertz fiber-based TOPAS extruded from a 3D printer using a metal 3D printed nozzle," Photon. Res., vol. 9, no. 8, pp. 1513–1521, 2021.
21. Z. Du et al., "Highly birefringent hollow-core anti-resonant terahertz fiber with a thin strut microstructure," Opt. Exp., vol. 30, no. 3, pp. 3783–3792, 2022.
22. J.-Y. Lu et al., "Terahertz air-core microstructure fiber," Appl. Phys. Lett., vol. 92, no. 6, 0641050–0641053, 2008.
23. M. M. Nazarov et al., "Eight-capillary cladding THz waveguide with low propagation losses and dispersion," IEEE Trans. Terahertz Sci., vol. 8, no. 2, pp. 183–191, 2018.
24. J. Sultana et al., "Exploring low loss and single mode in antiresonant tube lattice terahertz fibers," IEEE Access, vol. 8, pp. 113309–113317, 2020.
25. J. Sultana et al., "Hollow core inhibited coupled antiresonant terahertz fiber: a numerical and experimental study," IEEE Trans. Terahertz Sci., vol. 11, no. 3, pp. 245–260, 2021.
26. S. Yang, X. Sheng, G. Zhao, S. Lou, and J. Guo, "3D printed effective single-mode terahertz antiresonant hollow core fiber," IEEE Access, vol. 9, pp. 29599–29608, 2021.
27. L. van Putten, J. Gorecki, E. Numkam Fokoua, V. Apostolopoulos, and F. Poletti, "3D-printed polymer antiresonant waveguides for short-reach terahertz applications," Appl. Opt., vol. 57, no. 14, pp. 3953–3958, 2018.
28. P. Uebel et al., "Broadband robustly single-mode hollow-core PCF by resonant filtering of higher-order modes," Opt. Lett., vol. 41, no. 9, pp. 1961–1964, 2016.
29. S. F. Busch, M. Weidenbach, M. Fey, F. Schäfer, T. Probst, and M. Koch, "Optical Properties of 3D Printable Plastics in the THz Regime and their Application for 3D Printed THz Optics," J Infrared Millim. TE, vol. 35, no. 12, pp. 993–997, 2014.
30. S. Li et al., "A 0.1 THz low-loss 3D printed hollow waveguide," *Optik*, vol. 176, pp. 611–616, 2019.
31. X. Lu et al., "Flexible ABS hollow waveguides with an inner copper coating for terahertz transmission," Opt. Laser Technol., vol. 148, pp. 1077001–1077007, 2022.

Authors and Affiliations

Lu Xue[1] · Xinzhi Sheng[1] · Qiyuan Mu[2] · Depeng Kong[2] · Zhaojin Wang[3] · Paul K. Chu[4] · Shuqin Lou[5]

✉ Shuqin Lou
shqlou@bjtu.edu.cn

[1] School of Physical Science and Engineering, Beijing Jiaotong University, Beijing 100044, China

[2] State Key Laboratory of Transient Optics and Photonics, Xi'an Institute of Optics and Precision Mechanics, Chinese Academy of Sciences, Xi'an 710119, China

[3] School of Physics and Optoelectronics Technology, Baoji University of Arts and Science, Baoji 721016, China

[4] Department of Physics, Department of Materials Science & Engineering, Department of Biomedical Engineering, City University of Hong Kong, Tat Chee Avenue, Kowloon, Hong Kong, China

[5] Key Laboratory of Communication and Information Systems, Beijing Municipal Commission of Education, School of Electronic and Information Engineering, Beijing Jiaotong University, Beijing 100044, China